ACS Photonics

pubs.acs.org/journal/apchd5 Article

Metasurface Optical Characterization Using Quadriwave Lateral Shearing Interferometry

Samira Khadir,* Daniel Andrén, Ruggero Verre, Qinghua Song, Serge Monneret, Patrice Genevet, Mikael Käll, and Guillaume Baffou*

Cite This: *ACS Photonics* 2021, 8, 603–613 Read Online

ACCESS | Metrics & More | Article Recommendations | Supporting Information

ABSTRACT: An optical metasurface consists of a dense and usually nonuniform layer of scattering nanostructures behaving as a continuous and extremely thin optical component with predefined phase, transmission and reflection profiles. To date, various sorts of metasurfaces (metallic, dielectric, Huygens-like, Pancharatman-Berry, etc.) have been introduced to design ultrathin lenses, beam deflectors, holograms, or polarizing interfaces. Their actual efficiencies depend on the ability to predict their optical properties and to fabricate nonuniform assemblies of billions of nanoscale structures on macroscopic surfaces. To further help improve the design of metasurfaces, precise and versatile postcharacterization techniques need to be developed. Today, most of the techniques used to characterize metasurfaces rely on light intensity measurements. Here, we demonstrate how quadriwave lateral shearing interferometry (QLSI), a quantitative phase microscopy technique, can achieve full optical characterization of metasurfaces of any kind, as it can probe the local phase imparted by a metasurface with high sensitivity and a spatial resolution that reaches the diffraction limit. As a means to illustrate the versatility of this technique, we present measurements on two types of metasurfaces, namely, Pancharatnam-Berry and effective-refractive-index metasurfaces, and present results on uniform metasurfaces, metalenses, and deflectors.

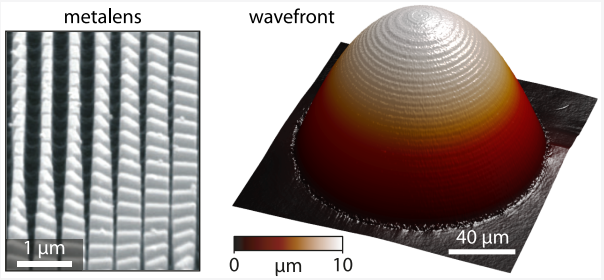

KEYWORDS: *metasurface, metalens, quadriwave lateral shearing interferometry, quantitative phase imaging*

An optical metasurface consists of a planar, dense distribution of scattering nanostructures with subwavelength sizes and interdistances behaving as a continuous and extremely thin optical component.[1−3] By tailoring the distribution, composition, and morphology of the nanostructures, usually called meta-atoms or meta-units, the effective optical properties of the metasurface can be spatially adjusted to control the transmitted and reflected light in amplitude, phase, and polarization. In particular, in order to construct efficient phase optical elements, typically lenses, one has to design meta-units that can cover the full $0 \rightarrow 2\pi$ phase-shift. This goal is impossible using meta-units consisting of single dipolar nanoparticles, the phase of which can only vary from 0 to π, since they behave as harmonic oscillators.[4] Thus, more complex nanostructures have to be used, either consisting of thick structures (like pillars around 1 μm in height), to favor the occurrence of retardation effects and deviate from a dipolar response, or using Huygens-metasurfaces,[5] based on shorter nanostructures that can reach a 2π phase shift when matching electric and magnetic dipole resonance frequencies. This past decade, many kinds of metasurfaces for different applications requiring flat optical components have been reported, such as metasurfaces to control reflection and refraction,[6−8] focus light and control its polarization,[9−11] produce a strong photonic spin Hall effect,[12,13] and project holographic images.[14,15]

Designing a metasurface with a specific functionality usually relies on predictions obtained from numerical simulations, including basic effective index analysis,[16] Huygens-metasurface designs,[5] and more sophisticated optimization procedures.[17−19] Novel and reliable optical characterization techniques would greatly facilitate a comparison between numerical predictions and actual metasurface measurements. Possible discrepancies and errors, originating either from the design or from fabrication imperfections, could be identified and compensated for to further improve device characteristics. To this end, several experimental characterization techniques have been utilized by the metasurface community, most of them relying on partial characterization or indirect measurements. Examples include measurements of polarization conversion efficiency, characterization of focal distance and

Received: November 5, 2020
Published: January 13, 2021

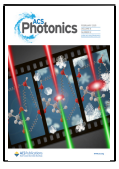

https://dx.doi.org/10.1021/acsphotonics.0c01707
ACS Photonics 2021, 8, 603–613

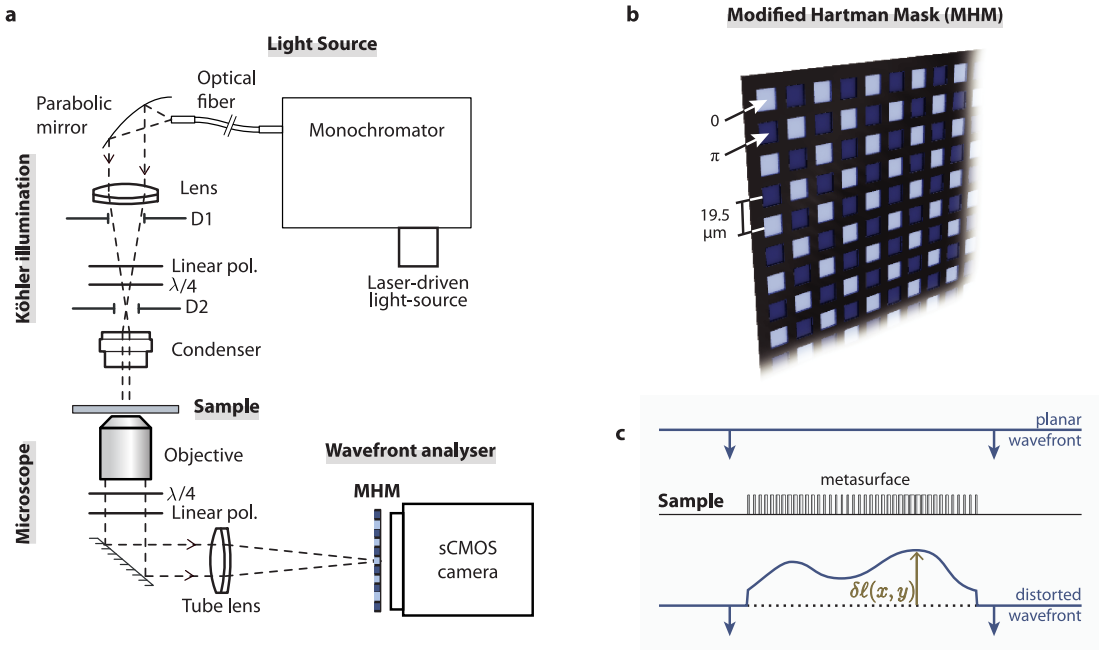

Figure 1. Working principle of QLSI. (a) Scheme of a QLSI microscope setup. A monochromator plasma source combined to a Köhler configuration illuminates the sample with a light beam controlled in wavelength, size, and numerical aperture. The light passing through the metasurface sample is collected by a microscope objective lens and sent to the QLSI wavefront analyzer, composed of a sCMOS camera equipped with a modified Hartman mask (MHM). (b) Geometry of the modified Hartman Mask. (c) Schematic showing the wavefront distortion $\delta l(x, y)$ experienced by a collimated light beam due to the presence of a metasurface.

point-spread-function in the case of metalenses,[20−22] and analysis of deflection angles for phase-gradient metasurfaces.[23] In optics, however, the most natural method to measure phase is interferometry, typically based on two light beams (one used as a reference) recombined to interfere on a detection plane, as is done in ref 24 to characterize plasmonic metasurfaces. Well-known drawbacks of the two-beam interferometry approach include noise and drift, leading to poor sensitivity, and complex setups that include two optical arms. To overcome these limitations, the three-beam method was proposed, where the third beam is used to analyze the environment and changes during an experiment,[25,26] although this approach makes the setup even more complicated. Traditional ellipsometry has also been used to characterize metasurfaces. Although this characterization technique is much more accessible, it is restricted to metasurfaces based on the manipulation of a phase difference between orthogonal light polarizations.[27] Scanning near-field optical microscopy (s-SNOM) provides subdiffraction resolution and allows for imaging of the near-field phase response of arbitrarily complex nanoparticle arrays,[28,29] but s-SNOM remains time-consuming and invasive. In particular, the coupling mechanisms between the near-field components and the nanoprobe tip crucially depend on the tip geometry, the light polarization, and the scanning mode, making a reliable prediction on the actual device efficiency difficult. More recently, Bouchal et al.[30] proposed an incoherent holographic imaging technique, but this method is restricted to the characterization of Pancharatman-Berry metasurfaces and meta-units or, more generally, orthogonal polarization components. Thus, the metasurface community still lacks an effective, reliable, and universal characterization technique that could enable parallel wafer-level testing for device reliability and detailed characterization of the device-phase profiles obtained directly after the metasurface plane.

In this Article, we propose to leverage on quadriwave lateral shearing interferometry (QLSI), a quantitative phase microscopy technique based on the use of a diffraction grating, to achieve optical characterization of arbitrary metasurfaces. Since QLSI measures wavefront distortion with sub-nm sensitivity and with high spatial resolution (down to the diffraction limit), it constitutes a powerful tool to characterize the actual transformation applied by a metasurface on a light beam. Moreover, its implementation is much more straightforward than any other phase characterization techniques of metasurfaces, since it is simply based on the integration of a diffraction grating with a camera, which should favor its wide dissemination. The first part of the Article introduces the working principle of QLSI and the experimental configuration. In the second part, we introduce the two families of metasurfaces that will be investigated throughout the Article and that are commonly used for realizing efficient dielectric metasurfaces, namely, effective-refractive-index (ERI) and Pancharatnam-Berry (PB) metasurfaces. Then, the use of QLSI to characterize metasurfaces is exemplified first on uniform meta-atom distributions, to explain the principle and demonstrate the reliability of the technique, and then on two practical cases: beam deflectors and metalenses.

QUADRIWAVE LATERAL SHEARING INTERFEROMETRY (QLSI)

QLSI Working Principle. QLSI is a quantitative phase imaging technique based on the use of a wavefront analyzer composed of two simple elements: a regular camera and a two-dimensional diffraction grating, separated by a millimetric distance from each other.[31] A good introduction to the working principle of QLSI can be found in ref 32. The diffraction grating (usually called a modified Hartmann mask, MHM) consists of a chessboard pattern of square transmitting

https://dx.doi.org/10.1021/acsphotonics.0c01707
ACS Photonics 2021, 8, 603−613

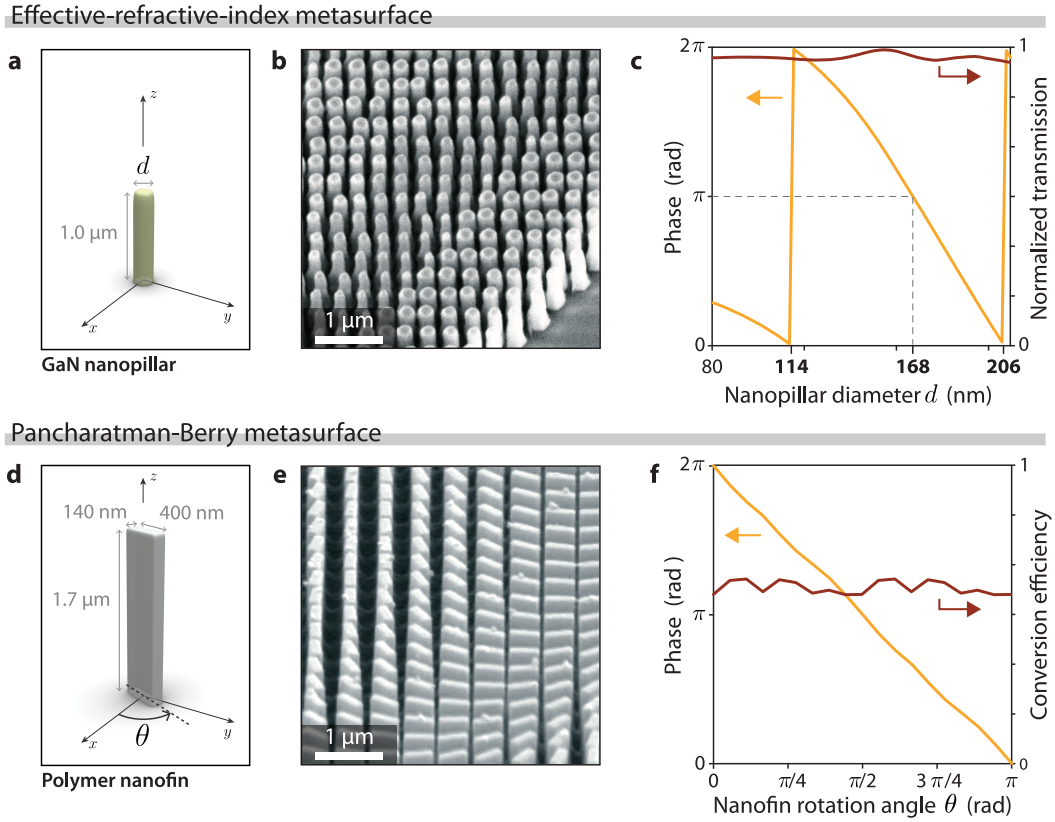

Figure 2. Metasurface sample descriptions. (a) Geometry of a GaN nanopillar. (b) SEM image of an ERI metasurface. (c) FDTD simulations, in periodic boundary conditions, of phase and transmittance of a GaN nanopillar array as a function of the cylinder diameter d, illuminated at λ = 600 nm. (d) Geometry of a polymer nanofin. (e) SEM image of PB metasurface. (f) FDTD Simulations, in periodic conditions, of phase and transmittance of a nanofin array with different rotation angles illuminated at λ = 532 nm.

units with alternating 0 and π phase shifts (Figure 1b). This geometry cancels the 0 order and mainly produces first diffraction orders in four directions. The four diffraction orders create four slightly shifted images on the camera that interfere to create a so-called interferogram. The grating-camera distance is not crucial. The technique works over a large range of distances, usually in the millimetric range. The larger the distance, the better the sensitivity.[33] The interferogram can be processed to retrieve both the intensity and the wavefront profiles $W(x, y)$ or, equivalently, the phase $\varphi(x, y)$ of an incoming light beam.[34] When mounted on a microscope, the measured wavefront profile is nothing but the optical path difference (OPD) image $\delta l(x, y)$ created by a sample in the object plane (Figure 1c). $\delta l = W$, and one usually defines

$$\delta l = \frac{\lambda_0}{2\pi}\varphi \tag{1}$$

where λ_0 is the illumination wavelength and $\varphi(x, y)$ is the phase delay experienced by a light beam crossing the sample in the object plane. The QLSI camera used in this study (Sid4 sC8 from Phasics S.A.) features an OPD sensitivity of 0.3 nm·$Hz^{-1/2}$ corresponding to around 3 mrad·$Hz^{-1/2}$ of phase delay in the visible range. Regarding the spatial (or lateral) resolution, it is limited by the diffraction limit associated with the numerical aperture of the objective lens, like in any optical microscopy technique. Importantly, QLSI benefits from the high sensitivity of interferometric methods but do not suffer from their usual drawbacks: it neither requires a reference beam, nor a complex alignment that might be sensitive to external perturbations. Compared with other existing interferometric techniques, this feature is what makes QLSI more accurate, reliable, and less likely to suffer from a signal that would come from illumination imperfection or instability. QLSI is a shot-noise limited technique. The relative positioning of the MHM with respect to the camera is done once and for all and is not sensitive to, for example, temperature variation, mechanical drift, or air flow. Most intensity and phase images presented in this study have been retrieved from interferogram images using a homemade algorithm. Over the past decade, several applications of QLSI have been demonstrated in biology and photonics, including cell imaging,[32] temperature imaging in nanoplasmonics,[35,36] 2D-material imaging,[37] and single nanoparticle optical characterization.[38] This work provides another application of QLSI for nanophotonics.

Experimental Setup. The experimental configuration of the optical microscope is depicted in Figure 1. The illumination part consists of a plasma laser-driven-light-source (EQ-99X from Energetiq Technologies) combined with a monochromator (Hypermonochromator, Mountain Photonics GmbH, purchased from Opton Laser International), enabling a variation of the wavelength over the visible range with a 6 nm bandwidth and a few mW of power. The use of an incoherent light source is preferable to avoid the appearance of fringes and speckles on the images. The optical fiber from the monochromator was positioned in a Köhler optical scheme to illuminate the sample with a sufficient degree of spatial coherence. This caution is a requirement in QLSI to achieve interferometric measurements despite the incoherent nature of

https://dx.doi.org/10.1021/acsphotonics.0c01707
ACS Photonics 2021, 8, 603−613

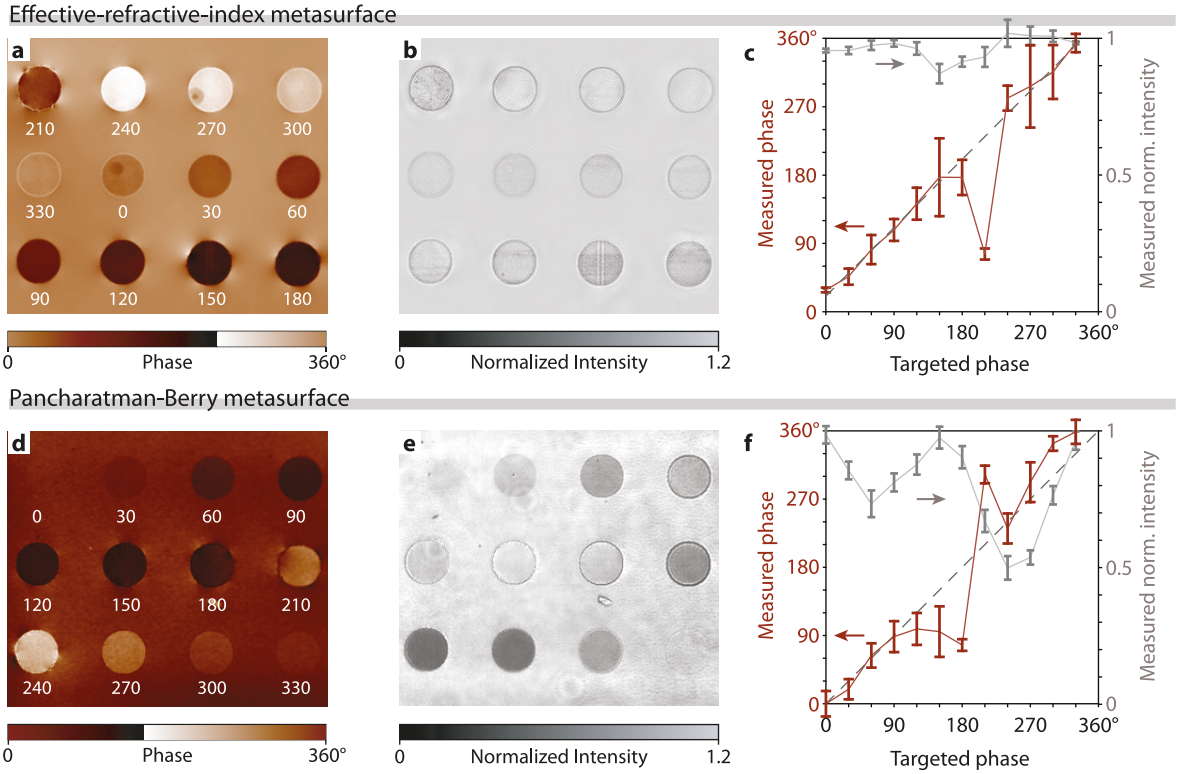

Figure 3. QLSI characterization of uniform metasurfaces. (a) Phase and (b) intensity images of 12 circular arrays (30 μm in diameter) of different GaN nanopillars, the sizes of which increase gradually from left to right and then from top to bottom. The targeted phase values are indicated on the phase image for each area, varying by steps of 30°. (c) Measurements of the phase and normalized intensity of the circular metasurfaces shown in images (a) and (b). (d) Phase and (e) intensity images of 12 circular arrays (30 μm in diameter) of different polymer nanofins, the orientation of which varies gradually by steps of 15° to make the phase vary by steps of 30°. The targeted phase values are indicated on the phase image for each area. (f) Measurements of the phase and normalized intensity of the circular metasurfaces shown in images (d) and (e).

the light source. In all the measurements, we used a 40× Olympus objective (LUCPLFLN40X), with a tube lens of focal distance 200 mm (magnification: 44×), except for the uniform metasurface characterization, where we used a 40× Nikon (S Fluor 40×), f = 200 mm, (magnification: 40×). The light passing through the sample is imaged by the microscope on the QLSI wavefront analyzer. Each measurement requires the acquisition of a reference image over a clear area (without any object) prior to taking an image with the object of interest within the field of view (in our case a metasurface). The reference is then subtracted from the object image to discard any imperfections of the incoming light beam. In the specific case of Pancharatnam-Berry metasurfaces characterization, a set of two optical polarizers and two quarter waveplates are added to the setup to study the device response in the standard circular cross-polarization configuration. We used a MHM provided by the Phasics company, implemented on a Zyla 5.5 camera (Andor, Sid4-sC8, Phasics).

Metasurfaces Principles and Designs. As a means to demonstrate the versatility of QLSI for metasurfaces characterization, two opposite families of metasurfaces have been investigated, namely, effective-refractive-index metasurfaces (Figure 2a), where the transmitted phase depends on the size of the meta-units, and Pancharatnam-Berry metasurfaces (Figure 2b), where the phase depends on the orientation of the meta-units.

Effective-Refractive-Index Metasurfaces. Effective-refractive-index (ERI) metasurfaces are often composed of a dense distribution of cylindrical pillars operating as independent Fabry−Perot resonators with a low quality factor (Figure 2a). The pillars are sufficiently tall to accommodate internal multilongitudinal-mode propagation, but remains sufficiently narrow to achieve large pillar density and prevent propagation of nonzero diffraction orders in free space or in the substrate.[39] The resulting effective refractive index of the pillar layer and, thus, the phase delay can be adjusted by varying the pillar diameter. In this study, we used a periodic square array of nanopillars made of GaN (see Figure 2b and Materials and Methods), 1 μm in height and with a 300 nm pitch, with diameters varying from 114 to 206 nm (see Figure 2c).

Pancharatman-Berry Metasurfaces. The Pancharatman-Berry (PB) phase is a kind of geometrical phase acquired by a light beam when passing through a birefringent medium.[40] PB metasurfaces are composed of asymmetric meta-units usually consisting of dielectric nanofins and providing the metasurface with birefrigent properties (Figure 2b).[20,41,42] To achieve maximum efficiency, PB metasurfaces require the use of circularly polarized illumination and detection of the circularly polarized light with the opposite handedness (see linear polarizers and quarter waveplates in Figure 1). Thus, in this cross-polarization configuration, no light is supposed to be detected, except where the sample features some birefringence, that is, where PB meta-units are present. The action of the nanofin on a light beam can be simply modeled assuming the nanofins act as a polarizing plate associated with the following Jones matrix:

https://dx.doi.org/10.1021/acsphotonics.0c01707
ACS Photonics 2021, 8, 603−613

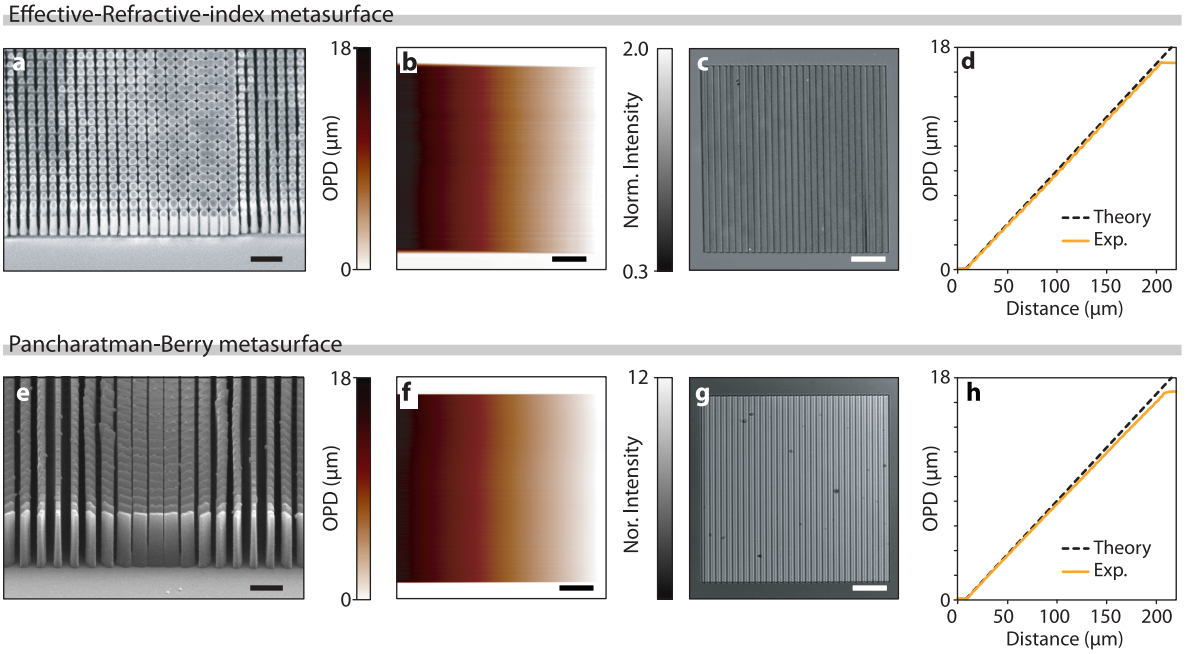

Figure 4. QLSI characterization of beam deflectors. (a) SEM image of a ERI deflecting metasurface (scale bar: 1 μm). (b) OPD image of the ERI beam deflector. (c) Associated normalized intensity image. (d) Averaged horizontal profile of (b) (solid line), compared with theory (dashed line). (e–h) Same as (a)–(d) for a PB beam deflecting metasurface.

$$\Gamma(\beta) = \begin{pmatrix} e^{i\beta/2} & 0 \\ 0 & e^{-i\beta/2} \end{pmatrix} \quad (2)$$

where β characterizes the meta-atom anisotropy. In this case, the complex amplitude A of the detected light in the circular cross-polarized configuration is given by (see derivation in Supporting Information):

$$A(\theta) = ie^{2i\theta} \sin(\beta/2) \quad (3)$$

where θ is the angle of the nanofin and $\sin(\beta/2)$ is called the conversion efficiency. As expected, for nonbirefringent structures ($\beta = 0$), no light is detected ($A = 0$) due to the crossed polarization configuration in illumination and detection. The value of β depends on the morphology, which can be optimized at a given wavelength to approach as much as possible $\sin(\beta/2) = 1$, that is, $\beta = \pi$, which means that an ideal PB meta-unit should act as a half-wave plate ($\Gamma(\pi)$). In this study, we used nanofins made of a patternable polymer with a pitch of 500 nm (see Figure 2d–f and Materials and Methods).

The transmission of light with the opposite handedness is due to the presence of birefringent structures, and eq 3 indicates that the phase of this transmitted light is dictated by the orientation of the nanofins. Setting the nanofin angle to θ results in a change of the local geometric phase of 2θ, no matter the composition or the morphology of the nanofin, providing it has some anisotropy.

The phase of ERI and PB meta-units are adjusted by varying, respectively, their size and their angle. In most nanofabrication techniques, a diameter is more difficult to accurately control compared to an angle. For instance, different e-beam doses are markedly affecting the sizes of lithographically fabricated objects, but not their orientations. For this reason, ERI metasurfaces are particularly sensitive to nanofabrication inaccuracies. Any inaccuracy in the PB meta-atom size only affects the conversion efficiency ($\sin(\beta/2)$ in eq 3), that is, the transmitted intensity, not the phase shift. Here lies the benefit of PB metasurfaces. PB metasurfaces are also dispersiveless (i.e., achromatic) since the phase of $A(\theta)$ (eq 3) is wavelength-independent, unlike ERI metasurfaces. However, PB metasurfaces are not outperforming ERI metasurfaces in any aspect. The main limitation of PB metasurfaces is the necessity to work with circularly polarized light to achieve maximum efficiency. In the following, we illustrate and discuss the use of QLSI for these two families of metasurfaces.

RESULTS

Characterization of Uniform Metasurfaces. Figure 3 presents QLSI images of uniform metasurfaces. In both case studies (ERI and PB), 12 circular "phase-piston" metasurfaces have been imaged within a single field of view. Each metasurface corresponds to a given phase shift, varying gradually by steps of 30° to span the entire 2π range.

The case of ERI metasurfaces corresponds to Figure 3a–c. The phase shifts are uniform over each disc, and the values are reported in Figure 3c. The agreement with the targeted phase is very good, except for phase shifts close to π. This issue is expected: QLSI primarily measures phase gradient images over x and y directions. The phase image is subsequently reconstructed numerically from these two gradient images. When a phase jump close to π occurs between neighboring pixels in a gradient image, the phase reconstruction algorithm cannot really know if the phase is actually decreasing or increasing and may assign a phase gradient of $\pm\pi$, the sign of which is highly noise-dependent. This random sign attribution can create some rendering issues, such as discontinuities and singularities in the phase image, like in the top-left area of Figure 3a. However, this issue is not expected to occur for most metasurface characterizations, as metasurfaces rarely exhibit phase steps of π and generally rather consist of regular and smooth variations of phase over space (see the metalens and metagradient characterization hereinafter). This π phase

https://dx.doi.org/10.1021/acsphotonics.0c01707
ACS Photonics 2021, 8, 603–613

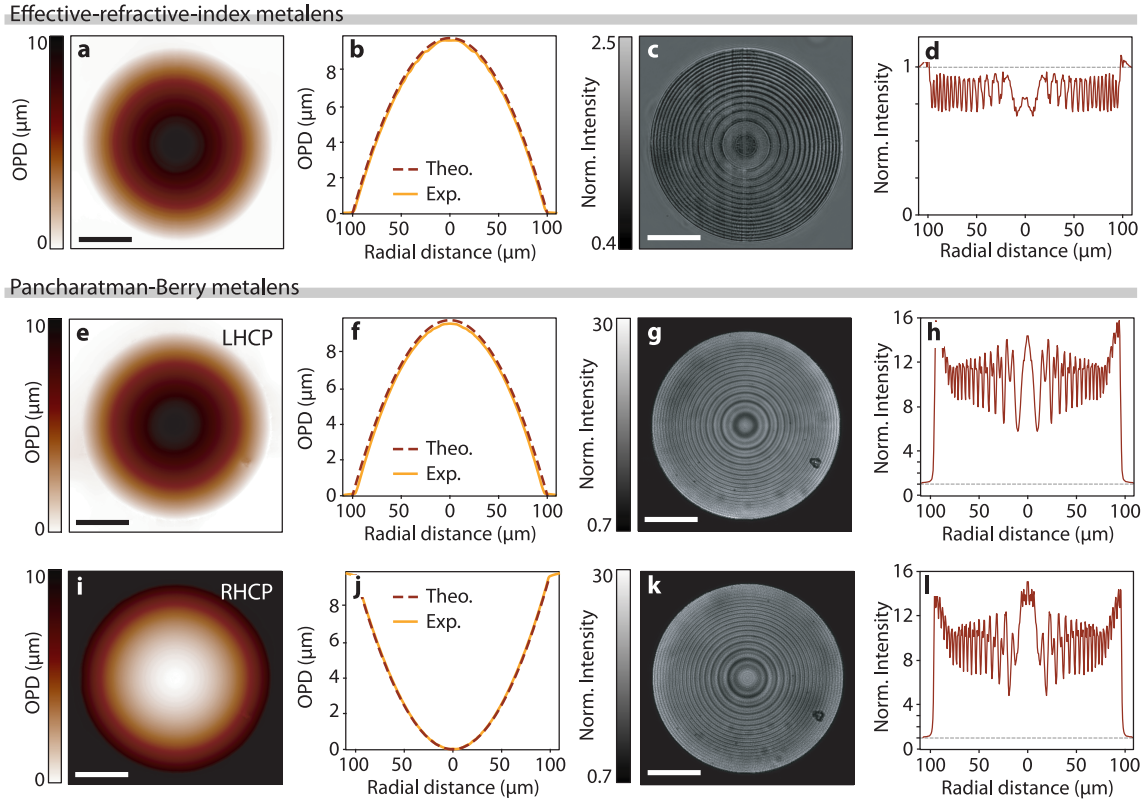

Figure 5. QLSI characterization of metalenses. (a) OPD images of the ERI metalens recorded by QLSI, along with its (b) radially averaged profile. (c) Normalized intensity image recorded by QLSI, associated with image (a), along with its (d) radially averaged profile. (e–h) Same as (a–d), for the PB metalens illuminated by a left-handed circular polarization (LHCP) beam. (i–l) Same as (e–h), the PB metalens illuminated by a RHCP beam. Scale bars for QLSI images: 50 μm.

step issue with QLSI has never been the subject of any particular study, as it rarely causes a problem: Objects typically studied by QLSI are usually smooth in phase, without phase discontinuities. We are not aware of alternative retrieval algorithms that could solve the problem. Nevertheless, this issue is certainly worthy of future attention since an improved phase retrieval algorithm able to deal with this current limitation would not only allow a more efficient characterization of metasurfaces, but also advance the QLSI technique in itself. Finally, QLSI also enables the reconstruction of the intensity image from the interferogram image. The normalized intensity image is displayed in Figure 3b, and measurements are reported in Figure 3c, which has to be compared with Figure 2c. This transmission of the metasurfaces is close to theoretical prediction (Figure 2c.), that is, quite constant upon varying the nanopillar diameter.

The case study of PB uniform metasurfaces is presented in Figures 3d–f. The sample contained 12 uniform and circular metasurfaces, in which the nanofin angle varied from one metasurface to another by increments of 15° to generate phase increments of 30° and cover the full 2π phase-shift. The circular areas observed in the images were surrounded by a uniform sea of fins oriented as in the 0° area, as a means to get nonzero light intensity outside the circular areas and also to have a nearby blank area with some transmitted light to acquire the reference image. The absence of a layer of PB meta-units around the metasurface would have resulted in a zero light intensity background, which is likely to create large noise on the image and even rendering issues upon reconstruction of the phase image. The phase values are reported in Figure 3f, with a good agreement with theory, except, again, when the phase is close to π, for the reason mentioned above. The normalized intensity image is displayed in Figure 3e and measurements are reported in Figure 3f, which have to be compared with Figure 2f. The transmission of the metasurfaces is not as uniform as expected upon varying the nanofin angle. This discrepancy can result from a near-field interaction between neighboring fins or possibly from some misalignment of the illumination and detection polarizing plates.

Characterization of Beam Deflectors. We now focus the study on a textbook case that is a beam deflecting or beam steering metasurface.[6,23,43,44] Again, we studied deflectors made of both ERI and PB metasurfaces. The devices have been designed to deflect light on the air side at a fixed angle of $\theta = 5°$. Considering (Oy) as the direction of deflection, the theoretical OPD reads

$$\delta l(y) = yn \sin(\theta) \tag{4}$$

where n is the refractive index of the medium ($n = 1$ in our case).

Experimental results are presented in Figure 4. SEM images (Figure 4a,e) detail gradual distribution of meta-units at the nanoscale. OPD images (Figure 4b,f) display the expected linear gradient of phase, in very good agreement with theory (Figures 4d,h). No fitting parameter has been introduced, except an arbitrary OPD offset. Also, no nanostructuration/roughness is included in the theoretical curve, which is only a linear function. Intensity images (Figure 4c,g) display some nonuniformities but do not noticeably affect the phase gradient.

https://dx.doi.org/10.1021/acsphotonics.0c01707
ACS Photonics 2021, 8, 603–613

Characterization of Metalenses. We focus now on the most common application of a metasurface, which is the metalens. We studied equivalent ERI and PB metalenses, designed with a fixed radius of $R = 100\ \mu$m and a focal length of $f = 500\ \mu$m (NA ~ 0.2). The theoretical OPD profile of such lenses is given by

$$\delta l(r) = \mp\sqrt{(r^2 + f^2)} + C \tag{5}$$

where r is a radial coordinate and C is a constant. The signs "−" or "+" correspond to convergent or divergent metalenses, respectively.

Figure 5a−d presents results on the characterization of an ERI metalens using QLSI. The radially averaged OPD profile (Figure 5b) shows a perfect agreement with theory (see eq 5). In all the numerical plots of Figure 5, no fitting parameter has been used, except the offset C in eq 5. The intensity profile (Figure 5d) is not perfectly uniform, exhibiting spatial variations in agreement with Figure 3c.

Figure 5e−l presents results on the characterization of a PB metalens. Again, phase measurements (Figure 5e) perfectly match theoretical predictions (Figure 5f). Interestingly, for PB metalenses, reversing the handedness of both the illumination and detection circular polarizations leads to a metalens with the opposite focal length $-f$.[11] This effect is indeed observed and characterized in Figure 5i, which reproduces the characteristics of a diverging lens in excellent agreement with theoretical predictions (Figure 5j). Just like with the ERI metalens, unexpected features are observed in the transmission profiles (Figure 5h,l): While theory predicts a transmission that is independent of the fin orientation (see eq 3), variations are observed throughout the metalens in agreement with Figure 3f. We evidence here that this nonuniform transmittance does not affect the quality of the phase profile.

Measurements of Zernike moments is common to characterize the aberrations of an optical system with circular pupils.[45,46] We explain hereinafter how QLSI can efficiently measure Zernike moments of metasurfaces. The Zernike polynomials Z_n^m are defined over the unit disk $r \in [0, 1]$, $\phi \in [0, 2\pi]$ as

$$Z_n^m(r, \theta) = R_n^m(r)e^{im\phi} \tag{6}$$

n and m are integers, following the restrictions $n \geq 0$, $0 \leq m \leq n$, and m of the same parity as n. $R_n^m(r)$ are polynomials with real coefficients, called the radial Zernike polynomials. For instance, $R_1^1(r) = r$, $R_2^0(r) = 2r^2 - 1$, and $R_2^2(r) = r^2$. Any smooth, real function F defined over a disc can be written as a linear combination of Zernike polynomials $(Z_n^m)_{n,m\in N}$, which form an orthonormal image basis:

$$F = \frac{1}{2}\sum_{n,m} c_{n,m}Z_n^m + c_{n,m}^* Z_n^{-m} \tag{7}$$

$c_{n,m}$ are complex coefficients called the complex Zernike moments of the image. The first elements of the Zernike basis, corresponding to the lowest spatial frequencies of the image, are represented in Figure 6a. Calculation of the moments of an image, such as the phase image represented in Figure 5a,e,i, requires to precisely define the center and the radius of the disc over which the moments have to be calculated. Then, the Zernike moments can be retrieved using

$$c_{n,m} = \frac{2(n+1)}{\pi\epsilon_m}\int_0^{2\pi}\int_0^1 F(r, \phi)Z_n^m(r, \phi)r\ \mathrm{d}r\ \mathrm{d}\phi \tag{8}$$

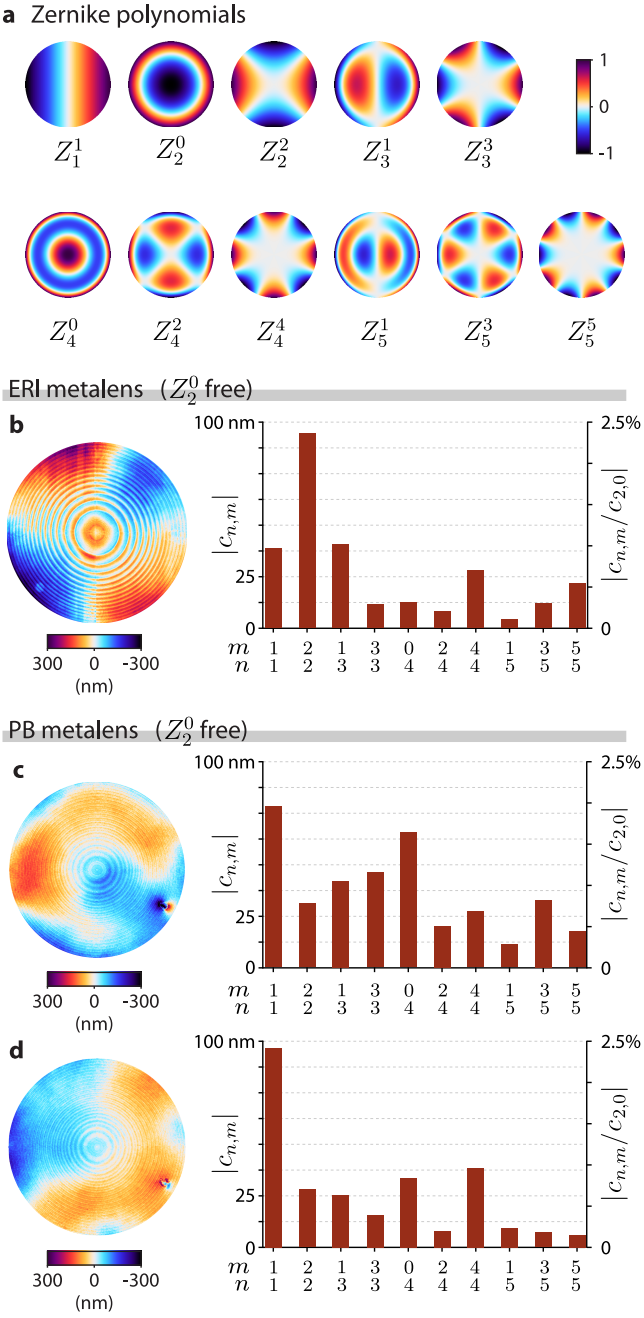

Figure 6. QLSI and Zernike analysis of metalenses. (a) Numerical simulations of the real parts of Zernike polynomials up to $n = 5$. (b) (Left) Optical thickness of an ERI metalens, from which the Zernike mode Z_2^0 was subtracted, highlighting the lens aberrations and imperfections. (Right) Measurements of the Zernike moments up to $n = 5$. (c) (Left) Optical thickness of a PB metalens from which the Zernike mode Z_2^0 was subtracted. (Right) Measurements of the Zernike moments up to $n = 5$. (d) Same as (c) for the opposite circularly polarized illumination handedness.

where $\epsilon_m = 2$ for even m values and $\epsilon_m = 1$ for odd m values: $\epsilon_m = 2 - \mathrm{modulo}(m, 2)$.

$Z_1^1(r,\phi) = re^{i\phi}$ represents a tilt over the direction ϕ. This moment is particular and requires some comments. First, the moment does not depend on the center of the disc on which the moment is calculated, contrary to all the other moments. Second, this moment is not really important for the characterization of the metalens as it affects neither the point

https://dx.doi.org/10.1021/acsphotonics.0c01707
ACS Photonics 2021, 8, 603−613

spread function (PSF) nor the efficiency of the metalens. The effect will only be a shift of the PSF. For these reasons, the tilt moment $c_{1,1}$ is of lesser interest compared to the other moments.

The second polynomial that requires attention, especially for a metalens, is $Z_2^0(r,\phi) = 2r^2 - 1$. When applied to an image obtained with an imaging system, Z_2^0 normally corresponds to the aberration called defocus. But when characterizing a lens, it is nothing but the moment corresponding to the phase profile of the lens itself, at least at the first order. Besides, the focal length of the metalens is linked to the Z_2^0 moment by the expression (see derivation in Supporting Information):

$$f = -\frac{R_Z^2}{4c_{2,0}} \tag{9}$$

R_Z^2 is the radius of the disc over which the Zernike moment $c_{2,0}$ is calculated. Ideally, it should be the radius of the metalens so that the full surface of the metalens is characterized. Note that the phase profile of the lens is hyperbolic (see eq 5), while Z_2^0 is parabolic. Thus, the fit is not perfect unless one has $R \ll f$, which is usually the case. In that case, one can assume a first order approximation of eq 5 giving a parabolic profile. eq 9 was derived using this approximation (see Supporting Information).

The following Zernike moments, $c_{2,2}$, $c_{3,1}$, $c_{3,3}$, ..., are estimations of deviations from the perfect parabolic profile of Z_2^0. These deviations can come from imperfections of the metalens. It can also come from imperfections of the illumination in case polarization matters (like with PB metasurfaces). $c_{n,0}$ can also come from the deviation of the hyperbolic profile from a parabolic profile, especially when the radius of the metalens is not significantly smaller than the focal length, that is, for metalenses with large numerical apertures.

Figure 6b(left) displays the optical thickness of an ERI metalens measured by QLSI, from which the measured Z_2^0 polynomial has been removed as a means to highlight the imperfections. A dominant Z_2^2 aberration is observed, corresponding to astigmatism. This dominant aberration is also evidenced in Figure 6b(right) reporting all the Zernike moments. All the other moments are very small, smaller than 1% of the (2, 0) moment. The moments' moduli are also plotted in nanometers to give an idea of the expected signal as compared with the camera sensitivity. Since QLSI sensitivity is around 1 nm, all the Zernike moments reported in Figure 6b(right) are well above the sensitivity of the technique, albeit very small, and do not correspond to measurement noise. All these aberrations come from the metalens only and are not supposed to come from any phase imperfection of the incoming light. Imperfections of the incoming light are unavoidable, but one gets rid of them in QLSI by subtracting a reference image.

Figure 6c,d addresses the case of a PB metalens, used as a convergent (Figure 6c) or divergent (Figure 6d) lens by rotating the circular polarizations. The difference with ERI metasurfaces is here that the Zernike moments can also depend on the light beam quality: any nonuniform deviation from a perfect circular polarization over the field of view may result in additional phase nonuniformity. The acquisition of a reference image may not compensate for this problem. Thus, the measured Zernike moments characterize both the light beam and the metalens and cannot be only attributed to metalens aberrations. This rule applies any time the polarization (linear or circular) matters for the characterization of metalenses, but can be more problematic for PB metasurfaces because perfectly circular polarizations are more complicated to achieve compared with linear polarizations. Any QLSI experiment on PB metasurfaces investigating high-order Zernike coefficients has to carefully set the circular polarizations in illumination and detection in order to faithfully probe the metalens quality and not something else. If a doubt regarding the beam quality persists, we recommend characterizing the metasurface at different positions within the field of view of the microscope by moving the sample holder to acquire one image in each quadrant, for instance. If the measured aberrations remain the same, then they are an intrinsic characteristic of the beam. If the aberrations are position-dependent, then the polarization uniformity of the beam has to be improved.

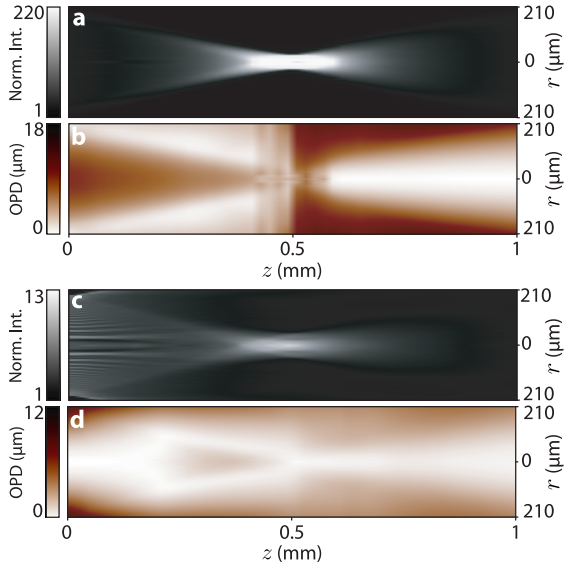

Figure 7. QLSI measurements of light propagation after a PB metalens. (a, b) LHCP/RHCP and (b, c) RHCP/LHCP configurations: (a) and (c) are intensity measurements and (b) and (d) are OPD measurements.

QLSI imaging is not limited to the focus plane. The technique can image the phase profile anywhere in space. In particular, QLSI can also characterize the light propagation in phase and intensity after crossing the metasurface as a means to better characterize the action of a metasurface. For this purpose, we translated the objective lens along its optical axis (Oz) and acquired several images as a function of its position along Oz. An equivalent option could have been to translate the sample along Oz. The intensity image presented in Figure 7a confirms that the light beam exiting the metalens is focused at a distance that corresponds to the focal length ($f = 500\ \mu$m). The OPD distribution (Figure 7b) exhibits an inversion of the contrast at the focal point corresponding to a phase shift of π. This phenomenon is known as the Gouy phase shift.[47] The tiny instabilities of the OPD image close to the focus spot, observed in Figure 7b, result from the lack of spatial coherence: At the location of the focus spot, the metalens images the source, which is in our experiment the exit of the optical fiber of the monochromator that is not spatially coherent. QLSI performs less well in this condition. In practice, the image of the light source should be sent to infinity and not imaged. Figure 7c,d reports measurements using the

https://dx.doi.org/10.1021/acsphotonics.0c01707
ACS Photonics 2021, 8, 603−613

reverse circular polarization configuration, where the metalens acts as a divergent lens. Regarding the light intensity (Figure 7c), it is vanishing upon propagation due to the divergence of the beam, with a residual, weak converging beam (1 order of magnitude lower than for the convergent lens) due to some imperfection of the illumination leading to a leakage of copolarized light. Regarding the phase profile (Figure 7d), the region 0−100 μm away from the metasurface clearly exhibits a diverging behavior, as the phase profile is convex and spreading out.

CONCLUSION

We have demonstrated how quadriwave lateral shearing interferometry (QLSI) can fully characterize the optical properties of metasurfaces in a simple, versatile, and accurate way. To illustrate the versatility of QLSI for metasurface metrology, we presented measurements on effective-refractive-index and Pancharatman-Berry metasurfaces. We highlighted the benefits of the techniques, but also the limitations, in particular, when dealing with local π phase steps. We also introduced the possibility and tested the capability of QLSI to measure metasurface imperfections using a Zernike polynomial approach. For the sake of clarity and conciseness, all the results presented in this study were restricted to the particular wavelength for which the metasurfaces were designed. However, nothing prevents one from performing measurements at other wavelengths, for instance, to quantify chromatic aberration using the Zernike polynomial methodology. This is possible since QLSI is an achromatic technique that can efficiently work over the whole spectral band of the associated camera, including measurements using white light. Furthermore, although we focused on metasurfaces a few hundred microns in diameter, the QLSI technique is well-suited to characterize much larger objects, including optical components several inches large.

Our aim with this article is to provide the nanophotonics community with a comprehensive guide to take the best of QLSI to the field of metasurfaces. Noteworthily, so far, quantitative phase imaging (QPI) techniques have been mostly developed and used in biology for imaging cells in culture. The interest of phase microscopy in biology lies in that cells are rather transparent objects, so that phase imaging gives much better contrast compared with regular intensity imaging. But the phase of light is first of all a physical quantity, and it is therefore quite surprising that QPI techniques have not gained wider use in the physics community. We predict QLSI is on the verge to change this and become a tool of predilection, in particular, in nanophotonics, especially thanks to unequaled advantages, namely, its compactness, high spatial resolution (down to the diffraction limit), high sensitivity (smaller than 1 nm), and quantification capabilities. All these benefits are important requirements for accurate and facile characterization of nanoscale components. Furthermore, QLSI is compatible with commercial microscopes available in almost any optics laboratory. For these reasons, we believe that QLSI has the potential to become a gold standard in nanophotonics metrology, and this Article is intended to push in that direction.

MATERIALS AND METHODS

ERI Metasurface Fabrication. Effective-refractive-index metasurfaces were made of square periodic arrays of GaN pillars, 1 μm in height, 300 nm pitch. They have been revealed by patterning a 1 μm thick GaN layer grown on a double-sided polished c-plan sapphire substrate using a Molecular Beam Epitaxy (MBE) RIBER system. Conventional electron beam lithography (EBL) was used to expose a double layer of ∼200 nm PMMA resist (495A4) spin-coated on the GaN thin-film and then baked on a hot plate at 125 °C. E-beam resist exposure was then performed at 20 keV (using a Raith ElphyPlus, Zeiss Supra 40), followed by PMMA development using a 3:1 IPA:MIBK solution. After development, a 50 nm layer of Ni was deposited using e-beam evaporation to perform a metallic film liftoff by immersing the sample into acetone solution for 2 h. The resulting Ni pattern was utilized as a hard mask during the reactive ion etching (RIE, Oxford system with a plasma composed of Cl_2, CH_4, Ar gases, with flows of 13, 2, and 2 sccm, respectively) to transfer the pattern in the GaN layer. Finally, the Ni hard mask on the top of GaN nanopillars was removed using chemical etching with a 1:2 HCl/HNO_3 solution. ERI metasurfaces have been designed to be used at a wavelength of 600 nm.

PB Metasurface Fabrication. We fabricated the PB metasurfaces using a novel approach based on the use of a patternable polymer (ma-N 2410, Micro Resist Technology GmbH, Germany) as the metasurface building material itself. The fabrication process is described in detail in ref 48. This fabrication technique allows for a facile route to make large-scale, high efficiency gradient metasurfaces. The constituent meta-units are freestanding nanofins with the dimension 400 × 140 × 1700 nm (Figure 2), which when placed in a square lattice with a 500 nm period, present a polarization conversion efficiency of $\sin(\beta/2) \approx 50\%$ at the operating wavelength of 530 nm. Using this type of metasurface building block, a hyperbolic lens with a focal length of 500 μm as well as a linear phase gradient metasurface were built. In the case of uniform metasurfaces and deflectors (but not in the case of metalenses), the metasurfaces were surrounded by a uniform sea of fins as a means to have light transmission also around the metasurfaces. All PB metasurfaces have been designed to be used at a wavelength of 532 nm.

ASSOCIATED CONTENT

Supporting Information

The Supporting Information is available free of charge at https://pubs.acs.org/doi/10.1021/acsphotonics.0c01707.

Complex transmittance for PB metasurface (eq 3) and a demonstration of the relation between the focal length of a metalens and the $c_{2,0}$ Zernike moment of its phase image (eq 9) (PDF)

AUTHOR INFORMATION

Corresponding Authors

Samira Khadir − *Université Cote d'Azur, CNRS, CRHEA, Sophia Antipolis 06560, Valbonne, France; Institut Fresnel, CNRS, Aix Marseille University, Marseille 13013, France;* orcid.org/0000-0002-2280-4099; Email: samira.khadir@crhea.cnrs.fr

Guillaume Baffou − *Institut Fresnel, CNRS, Aix Marseille University, Marseille 13013, France;* orcid.org/0000-0003-0488-1362; Email: guillaume.baffou@fresnel.fr

https://dx.doi.org/10.1021/acsphotonics.0c01707
ACS Photonics 2021, 8, 603−613

Authors

Daniel Andrén − *Department of Physics, Chalmers University of Technology, 412 96 Göteborg, Sweden;* orcid.org/0000-0003-0682-5129

Ruggero Verre − *Department of Physics, Chalmers University of Technology, 412 96 Göteborg, Sweden;* orcid.org/0000-0001-8337-9009

Qinghua Song − *Université Cote d'Azur, CNRS, CRHEA, Sophia Antipolis 06560, Valbonne, France*

Serge Monneret − *Institut Fresnel, CNRS, Aix Marseille University, Marseille 13013, France*

Patrice Genevet − *Université Cote d'Azur, CNRS, CRHEA, Sophia Antipolis 06560, Valbonne, France*

Mikael Käll − *Department of Physics, Chalmers University of Technology, 412 96 Göteborg, Sweden;* orcid.org/0000-0002-1163-0345

Complete contact information is available at: https://pubs.acs.org/10.1021/acsphotonics.0c01707

Notes

The authors declare no competing financial interest.

■ ACKNOWLEDGMENTS

S.K., Q.S., and P.G. acknowledge financial support from the European Research Council (ERC) under the European Union's Horizon 2020 research and innovation programme (Grant Agreement FLATLIGHT No. 639109 and Grant Agreement i-LiDAR No. 874986), and from the French government, through the UCAJEDI Investments in the Future project managed by the National Research Agency (ANR) with the reference number ANR-15-IDEX-01. D.A., R.V., and M.K. would like to thank the Knut and Alice Wallenberg Foundation, the Swedish Foundation for Strategic Research and the Excellence Initiative Nano at Chalmers University of Technology. This work was partially performed at Myfab Chalmers. The authors thank B. Wattellier and R. Laberdesque for helpful discussions.

■ REFERENCES

(1) Chen, W. T.; Zhu, A. Y.; Capasso, F. Flat Optics with Dispersion-Engineered Metasurfaces. *Nat. Rev. Mater.* **2020**, *5*, 604−620.

(2) Ding, F.; Pors, A.; Bozhevolnyi, S. I. Gradient metasurfaces: a review of fundamentals and applications. *Rep. Prog. Phys.* **2018**, *81*, 026401.

(3) Khorasaninejad, M.; Capasso, F. Versatile Multifunctional Photonic Components. *Science* **2017**, *358*, No. eaam8100.

(4) Kats, M. A.; Yu, N.; Genevet, P.; Gaburro, Z.; Capasso, F. Effect of Radiation Damping on the Spectral Response of Plasmonic Components. *Opt. Express* **2011**, *19*, 21748.

(5) Decker, M.; Staude, I.; Falkner, M.; Dominguez, J.; Neshev, D. N.; Brener, I.; Pertsch, T.; Kivshar, Y. S. High-Efficiency Dielectric Huygens' Surfaces. *Adv. Opt. Mater.* **2015**, *3*, 813−820.

(6) Yu, N.; Genevet, P.; Kats, M. A.; Aieta, F.; Tetienne, J.-P.; Capasso, F.; Gaburro, Z. Light Propagation with Phase Discontinuities: Generalized Laws of Reflection and Refraction. *Science* **2011**, *334*, 333.

(7) Ni, X.; Emani, N. K.; Kildishev, A. V.; Boltasseva, A.; Shalaev, V. M. Broadband Light Bending with Plasmonic Nanoantennas. *Science* **2012**, *335*, 427.

(8) Sun, S.; Yang, K.-Y.; Wang, C.-M.; Juan, T.-K.; Chen, W. T.; Liao, C. Y.; He, Q.; Xiao, S.; Kung, W.-T.; Guo, G.-Y.; et al. High-Efficiency Broadband Anomalous Reflection by Gradient Meta-Surfaces. *Nano Lett.* **2012**, *12*, 6223−6229.

(9) Niv, A.; Biener, G.; Kleiner, V.; Hasman, E. Propagation-invariant vectorial Bessel beams obtained by use of quantized Pancharatnam−Berry phase optical elements. *Opt. Lett.* **2004**, *29*, 238−240.

(10) Aieta, F.; Genevet, P.; Kats, M. A.; Yu, N.; Blanchard, R.; Gaburro, Z.; Capasso, F. Aberration-Free Ultrathin Flat Lenses and Axicons at Telecom Wavelengths Based on Plasmonic Metasurfaces. *Nano Lett.* **2012**, *12*, 4932−4936.

(11) Chen, X.; Huang, L.; Mühlenbernd, H.; Li, G.; Bai, B.; Tan, Q.; Jin, G.; Qiu, C.-W.; Zhang, S.; Zentgraf, T. Dual-polarity plasmonic metalens for visible light. *Nat. Commun.* **2012**, *3*, 1198.

(12) Yin, X.; Ye, Z.; Rho, J.; Wang, Y.; Zhang, X. Photonic Spin Hall Effect at Metasurfaces. *Science* **2013**, *339*, 1405.

(13) Ling, X.; Zhou, X.; Yi, X.; Shu, W.; Liu, Y.; Chen, S.; Luo, H.; Wen, S.; Fan, D. Giant photonic spin Hall effect in momentum space in a structured metamaterial with spatially varying birefringence. *Light: Sci. Appl.* **2015**, *4*, No. e290.

(14) Genevet, P.; Capasso, F. Holographic optical metasurfaces: a review of current progress. *Rep. Prog. Phys.* **2015**, *78*, 024401.

(15) Ren, H.; Briere, G.; Fang, X.; Ni, P.; Sawant, R.; Heron, S.; Chenot, S.; Vezian, S.; Damilano, B.; Brandli, V.; Maier, S. A.; Genevet, P. Metasurface orbital angular momentum holography. *Nat. Commun.* **2019**, *10*, 2986.

(16) Lalanne, P.; Astilean, S.; Chavel, P.; Cambril, E.; Launois, H. Design and fabrication of blazed binary diffractive elements with sampling periods smaller than the structural cutoff. *J. Opt. Soc. Am. A* **1999**, *16*, 1143.

(17) Yao, K.; Unni, R.; Zheng, Y. Intelligent nanophotonics: merging photonics and artificial intelligence at the nanoscale. *Nanophotonics* **2019**, *8*, 339−366.

(18) Campbell, S. D.; Sell, D.; Jenkins, R. P.; Whiting, E. B.; Fan, J. A.; Werner, D. H. Review of numerical optimization techniques for meta-device design. *Opt. Mater. Express* **2019**, *9*, 1842−1863.

(19) Molesky, S.; Lin, Z.; Piggott, A. Y.; Jin, W.; Vuckovic, J.; Rodriguez, A. W. Inverse design in nanophotonics. *Nat. Photonics* **2018**, *12*, 659−670.

(20) Liang, H.; Lin, Q.; Xie, X.; Sun, Q.; Wang, Y.; Zhou, L.; Liu, L.; Yu, X.; Zhou, J.; Krauss, T. F; Li, J. Ultrahigh Numerical Aperture Metalens at Visible Wavelengths. *Nano Lett.* **2018**, *18*, 4460−4466.

(21) Colburn, S.; Zhan, A.; Majumdar, A. Metasurafce Optics for Full-Color Computational Imaging. *Sci. Adv.* **2018**, *4*, No. eaar2114.

(22) Banerji, S.; Meem, M.; Majumder, A.; Vasquez, F. G.; Sensale-Rodriguez, B.; Menon, R. Imaging with flat optics: metalenses or diffractive lenses? *Optica* **2019**, *6*, 805−810.

(23) Khorasaninejad, M.; Crozier, K. B. Silicon nanofin grating as a miniature chirality-distinguishing beam-splitter. *Nat. Commun.* **2014**, *5*, 5386.

(24) Babocký, J.; Křížová, A.; Štrbková, L.; Kejík, L.; Ligmajer, F.; Hrtoň, M.; Dvořák, P.; Týč, M.; Čolláková, J.; Křápek, V.; et al. Quantitative 3D Phase Imaging of Plasmonic Metasurfaces. *ACS Photonics* **2017**, *4*, 1389−1397.

(25) Azari, A.; Mohajerani, E.; Abedi, Z.; Shams, A. Interferometry technique to eliminate noise in interference data based on a Mach−Zehnder interferometer. *Appl. Opt.* **2014**, *53*, 1734−1738.

(26) Ollanik, A. J.; Hartfield, G. Z.; Ji, Y.; Robertson, J. T.; Islam, K.; Escarra, M. D. Characterization of Dynamic and Nanoscale Materials and Metamaterials with Continuously Referenced Interferometry. *Adv. Opt. Mater.* **2019**, *7*, 1901128.

(27) Chen, W.-Y.; Lin, C.-H.; Chen, W.-T. Plasmonic phase transition and phase retardation: essential optical characteristics of localized surface plasmon resonance. *Nanoscale* **2013**, *5*, 9950−9956.

(28) Neuman, T.; Alonso-González, P.; Garcia-Etxarri, A.; Schnell, M.; Hillenbrand, R.; Aizpurua, J. Mapping the near fields of plasmonic nanoantennas by scattering-type scanning near-field optical microscopy. *Laser Photonics Rev.* **2015**, *9*, 637−649.

(29) Bohn, B. J.; Schnell, M.; Kats, M. A.; Aieta, F.; Hillenbrand, R.; Capasso, F. Near-Field Imaging of Phased Array Metasurfaces. *Nano Lett.* **2015**, *15*, 3851−3858.

(30) Bouchal, P.; Dvořák, P.; Babocký, J.; Bouchal, Z.; Ligmajer, F.; Hrtoň, M.; Křápek, V.; Faßbender, A.; Linden, S.; Chmelík, R.; et al. High-Resolution Quantitative Phase Imaging of Plasmonic Metasurfaces with Sensitivity down to a Single Nanoantenna. *Nano Lett.* **2019**, *19*, 1242−1250.
(31) Primot, J.; Guérineau, N. Extended Hartmann Test Based on the Pseudoguiding Property of a Hartmann Mask Completed by a Phase Chessboard. *Appl. Opt.* **2000**, *39*, 5715−5720.
(32) Bon, P.; Maucort, G.; Wattellier, B.; Monneret, S. Quadriwave lateral shearing interferometry for quantitative phase microscopy of living cells. *Opt. Express* **2009**, *17*, 13080−94.
(33) Primot, J.; Sogno, L. Achromatic three-wave (or more) lateral shearing interferometer. *J. Opt. Soc. Am. A* **1995**, *12*, 2679−2685.
(34) Bon, P.; Monneret, S.; Wattellier, B. Noniterative Boundary-Artifact-Free Wavefront Reconstruction from its Derivatives. *Appl. Opt.* **2012**, *51*, 5698−5704.
(35) Baffou, G.; Bon, P.; Savatier, J.; Polleux, J.; Zhu, M.; Merlin, M.; Rigneault, H.; Monneret, S. Thermal Imaging of Nanostructures by Quantitative Optical Phase Analysis. *ACS Nano* **2012**, *6*, 2452−2458.
(36) Robert, H. M. L.; Savatier, J.; Vial, S.; Verghese, J.; Wattellier, B.; Rigneault, H.; Monneret, S.; Polleux, J.; Baffou, G. Photothermal control of heat-shock protein expression at the single cell level. *Small* **2018**, *14*, 1801910.
(37) Khadir, S.; Bon, P.; Vignaud, D.; Galopin, E.; McEvoy, N.; McCloskey, D.; Monneret, S.; Baffou, G. Optical Imaging and Characterization of Graphene and Other 2D Materials Using Quantitative Phase Microscopy. *ACS Photonics* **2017**, *4*, 3130−3139.
(38) Khadir, S.; Andren, D.; Chaumet, P. C.; Monneret, S.; Bonod, N.; Käll, M.; Sentenac, A.; Baffou, G. Full optical characterization of single nanoparticles using quantitative phase imaging. *Optica* **2020**, *7*, 243−248.
(39) Genevet, P.; Capasso, F.; Aieta, F.; Khorasaninejad, M.; Devlin, R. Recent advances in planar optics: from plasmonic to dielectric metasurfaces. *Optica* **2017**, *4*, 139−152.
(40) Cohen, E.; Larocque, H.; Bouchard, F.; Nejadsattari, F.; Gefen, Y.; Karimi, E. Geometric phase from Aharonov−Bohm to Pancharatnam−Berry and beyond. *Nat. Rev.* **2019**, *1*, 437.
(41) Khorasaninejad, M.; Chen, W. T.; Devlin, R. C.; Oh, J.; Zhu, A. Y.; Capasso, F. Metalenses at Visible Wavelengths: Diffraction-Limited Focusing and Subwavelength Resolution Imaging. *Science* **2016**, *352*, 1190−1194.
(42) Wang, S.; Wu, P. C.; Su, V.-C.; Lai, Y.-C.; Chen, M.-K.; Kuo, H. Y.; Chen, B. H.; Chen, Y. H.; Huang, T.-T.; Wang, J.-H.; et al. A broadband achromatic metalens in the visible. *Nat. Nanotechnol.* **2018**, *13*, 227−232.
(43) Lin, D.; Fan, P.; Hasman, E.; Brongersma, M. L. Dielectric Gradient Metasurface Optical Elements. *Science* **2014**, *345*, 298−302.
(44) Pors, A.; Albrektsen, O.; Radko, I. P.; Bozhevolnyi, S. I. Gap Plasmon-Based Metasurfaces for Total Control of Reflected Light. *Sci. Rep.* **2013**, *3*, 2155.
(45) Lakshminarayanan, V.; Fleck, A. Zernike polynomial: a guide. *J. Mod. Opt.* **2011**, *58*, 545−561.
(46) Berto, P.; Philippet, L.; Osmond, J.; Liu, C. F.; Afridi, A.; Montagut Marques, M.; Molero Agudo, B.; Tessier, G.; Quidant, R. Tunable and Free-Form Planar Optics. *Nat. Photonics* **2019**, *13*, 649−656.
(47) Feng, S.; Winful, H. G. Physical origin of the Gouy phase shift. *Opt. Lett.* **2001**, *26*, 485−487.
(48) Andrén, D.; Martínez-Llinas, J.; Tassin, P.; Käll, M.; Verre, R. Large-Scale Metasurfaces Made by an Exposed Resist. *ACS Photonics* **2020**, *7*, 885−892.

https://dx.doi.org/10.1021/acsphotonics.0c01707
ACS Photonics 2021, 8, 603−613